

Mapping the magnetic field in the solar corona through magnetoseismology

YANG ZiHao¹, TIAN Hui^{1,2*}, TOMCZYK Steven³, MORTON Richard⁴,
BAI XianYong², SAMANTA Tanmoy^{5,6}, and CHEN YaJie^{1,7}

¹*School of Earth and Space Sciences, Peking University, Beijing 100871, China; huitian@pku.edu.cn;*

²*Key Laboratory of Solar Activity, National Astronomical Observatories, Chinese Academy of Sciences, Beijing 100012, China;*

³*High Altitude Observatory, National Center for Atmospheric Research, Boulder, CO 80307, USA;*

⁴*Department of Mathematics, Physics and Electrical Engineering, Northumbria University, Newcastle Upon Tyne NE1 8ST, UK;*

⁵*Department of Physics and Astronomy, George Mason University, Fairfax, VA 22030, USA;*

⁶*Johns Hopkins University Applied Physics Laboratory, Laurel, MD 20723, USA;*

⁷*Max Planck Institute for Solar System Research, 37077 Göttingen, Germany*

Received ; accepted

Magnetoseismology, a technique of magnetic field diagnostics based on observations of magnetohydrodynamic (MHD) waves, has been widely used to estimate the field strengths of oscillating structures in the solar corona. However, previously magnetoseismology was mostly applied to occasionally occurring oscillation events, providing an estimate of only the average field strength or one-dimensional distribution of field strength along an oscillating structure. This restriction could be eliminated if we apply magnetoseismology to the pervasive propagating transverse MHD waves discovered with the Coronal Multi-channel Polarimeter (CoMP). Using several CoMP observations of the Fe XIII 1074.7 nm and 1079.8 nm spectral lines, we obtained maps of the plasma density and wave phase speed in the corona, which allow us to map both the strength and direction of the coronal magnetic field in the plane of sky. We also examined distributions of the electron density and magnetic field strength, and compared their variations with height in the quiet Sun and active regions. Such measurements could provide critical information to advance our understanding of the Sun's magnetism and the magnetic coupling of the whole solar atmosphere.

Solar corona, Solar magnetic field, Waves, Magnetoseismology

Citation: Yang Z, Tian H, Tomczyk S, et al.,
Sci China Tech Sci xx, xxx (2020), doi: <https://doi.org/10.1007/s11431-020-1706-9>

1 Introduction

Originating from the solar interior, the solar magnetic field extends to the solar surface and couples different layers of the solar atmosphere (Figure 1). Because of this, information on the magnetic field of the whole atmosphere is required to study the interplay between the solar plasma and magnetic field. However, routine and reliable measurements of the solar magnetic field have only been achieved at the photospheric level (e.g., [1, 2]). We still do not have a precise knowledge of the magnetic field in the upper solar atmo-

sphere, especially the corona, which impedes our complete understanding of a wide range of phenomena including the solar cycle, solar eruptions and heating of the coronal plasma.

Without routine measurements of the coronal magnetic field, extrapolations from the observed photospheric magnetograms often serve as an important tool for reconstruction of coronal magnetic field structures (e.g., [3-7]). Extrapolation models can be classified into potential field, linear force-free field and non-linear force-free field extrapolations. Figure 1 shows an example of the global coronal magnetic field structures obtained from the most frequently used potential field

source surface (PFSS) model. In addition, magnetohydrostatic (e.g., [8, 9]) and magnetohydrodynamic (MHD) models (e.g., [10, 11]) have also been developed to reconstruct three-dimensional (3D) magnetic field structures in the solar atmosphere. Although widely used for investigations of the coronal magnetism, these models are highly dependent on various assumptions, which are not always valid on the Sun.

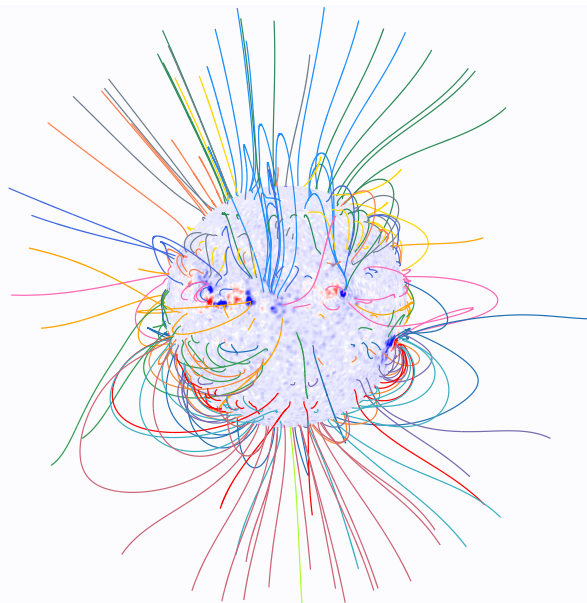


Figure 1 Global coronal magnetic field on Oct 14, 2016 obtained from the PFSS model. The colored lines represent selected magnetic field lines. The synoptic photospheric magnetogram used for the PFSS model is shown in the middle, and the red and blue patches represent different polarities of the longitudinal magnetic field.

Direct measurements of the coronal magnetic field through spectropolarimetric observations have been attempted in the past two decades. The linear polarization of some coronal forbidden lines is sensitive to the magnetic field orientation in the plane of sky (POS) (e.g., [12-14]), and the degree of linear polarization could be used to diagnose some magnetic structures such as flux ropes [15-17]. Due to the weak field in the corona, circular polarization signals associated with the longitudinal Zeeman effect are usually very weak. In order to measure the line-of-sight (LOS) component of the coronal magnetic field, often a long integration time is required to increase the signal-to-noise ratio (S/N) of the circular polarization data. Only a couple of successful measurements have been performed using this method [18, 19].

Besides spectropolarimetric measurements, several other techniques have also been developed to probe the coronal magnetic field. For instance, the standoff distance method could be used to infer the field strengths along the paths of shocks driven by fast coronal mass ejections (CMEs) [20].

Radio spectral observations of type III bursts, spike structures associated with type IV bursts and zebra patterns could also provide estimates of the magnetic field in the coronal source regions of the radio emission [21-23]. In addition, when the emission mechanisms are known, microwave imaging at one or more frequencies could be used to produce maps of the coronal magnetic field strength in limited regions [24-29]. More recently, the phenomenon of magnetic-field-induced transition (MIT) [30] has caught the attention of the solar physics community, and theoretical and laboratory investigations have demonstrated the potential of MIT lines in measurements of the coronal magnetic field [31-33].

Another frequently used approach for measurements of the coronal magnetic field is coronal seismology or magnetoseismology, which refers to magnetic field diagnostics based on observations of MHD waves or oscillations (e.g., [34]). For transverse kink oscillations, the magnetic field strengths in or outside oscillating structures could be derived if the local density is assumed or estimated [35-42]. However, these rare single-oscillation events are often related to flares or CMEs, and their observations can provide an estimate of only the average field strength or one-dimensional (1D) distribution of field strength along an oscillating structure. This restriction could be eliminated if we apply magnetoseismology to more ubiquitous and continuous oscillations or waves in the corona. At least two types of such oscillations/waves are known to exist in the corona: the decayless/persistent standing transverse waves in coronal loops observed through extreme-ultraviolet (EUV) imaging and spectroscopic observations [43-46], and the pervasive propagating transverse waves observed with the Coronal Multi-channel Polarimeter (CoMP, [47]) [48-53]. These ubiquitous oscillations/waves, especially the latter, are potentially important for continuous diagnostics of coronal magnetic field [51, 54]. By applying the technique of magnetoseismology to the pervasive propagating waves observed with CoMP, we could map the magnetic field in the corona. The first attempt was made for a trans-equatorial loop system, though the magnetic field magnitude was obtained at only a limited number of pixels in the bottom part of the loop system [55]. Recently, using CoMP observations on October 14, 2016, we managed to perform the first measurement of the global coronal magnetic field in the POS [56].

In this paper, we will present analysis results for more datasets using the same technique. We will also present maps of the POS magnetic field orientation measured from wave observations and the magnetic azimuth derived from linear polarization observations. In addition, we will examine distributions of the electron density and magnetic field strength, and compare their variations with height in the quiet Sun and

active regions.

2 Instruments and Data

The CoMP is a 20-cm aperture coronagraph mounted at Mauna Loa Solar Observatory in Hawaii. It can perform spectropolarimetric observations at infrared wavelengths. We used the data sampled at several wavelength positions across the spectral profiles of Fe XIII 1074.7 nm and 1079.8 nm on October 14, 2016 (dataset D1), November 3, 2016 (dataset D2) and March 20, 2017 (dataset D3). These three observations were taken under relatively good and stable observing conditions. The spatial sampling is $\sim 4.35''$. The field-of-view (FOV) is about 1.05-1.35 solar radii from the solar center. We used the Stokes-I profiles of the two lines for density diagnostics, the Stokes-I data of Fe XIII 1074.7 nm for wave tracking, and the Stokes Q and U data of Fe XIII 1074.7 nm for calculation of magnetic azimuth. The Doppler velocity and peak intensity were obtained through an analytical Gaussian fitting to the three-point intensity (Stokes-I) profile at each spatial pixel [57]. The details of the three observations are

summarized in Table 1. For dataset D1, intensity images of the two Fe XIII lines have been presented in our previous work [56]. Figure 2(B)-(C) and Figure 3(B)-(C) show the Fe XIII intensities for the other two datasets. Note that for datasets D2 and D3, we present results derived from only the good-quality data in parts of the global corona. We only show pixels where the Fe XIII 1074.7 nm peak intensity is higher than 1.0 ppm (millionth of the solar disk intensity). In addition, we excluded pixels where the phase speed (see below) exceeds 2000 km s^{-1} from the maps of phase speed and magnetic field strength.

For comparison, we also used the simultaneously obtained 19.3 nm images observed by the Atmospheric Imaging Assembly (AIA, [58]) on the Solar Dynamics Observatory (SDO). For dataset D1, again we refer the chosen AIA image to our previous work [56]. For dataset D2, we chose the AIA 19.3 nm image observed at 20:00:07 UT on November 3, 2016 (Figure 2(A)). For dataset D3, the AIA 19.3 nm image obtained at 19:00:18 UT on March 20, 2017 was used (Figure 3(A)). These images have a spatial sampling of $\sim 0.6''$.

Table 1 Details of the CoMP observations used in our study.

Datasets	Time range for density diagnostics	Frame number for density diagnostics	Time range for wave tracking/azimuth calculation	Frame number for wave tracking/azimuth calculation
D1 (October 14, 2016)	19:24 UT - 20:17 UT	1074.7 nm: 49 1079.8 nm: 10	20:39 UT - 21:26 UT	1074.7 nm: 94
D2 (November 3, 2016)	19:14 UT - 20:20 UT	1074.7 nm: 63 1079.8 nm: 12	20:34 UT - 21:37 UT	1074.7 nm: 125
D3 (March 20, 2017)	18:27 UT - 19:43 UT	1074.7 nm: 78 1079.8 nm: 14	19:53 UT - 20:44 UT	1074.7 nm: 101

3 Analysis results

3.1 Coronal magnetic field measurements through magnetoseismology

Previous CoMP observations have shown that the pervasive propagating transverse waves, manifested as propagating perturbations in the Fe XIII 1074.7 nm Doppler velocity sequences, often have a power spectrum peaked around 3.5 mHz (corresponding to a period of ~ 5 min) [48, 49, 51, 53]. These transverse waves are identified as kink or Alfvénic waves. Considering the lower-beta coronal environment and the moderate spatial resolution of CoMP ($\sim 9''$), an appropri-

ate expression of the wave phase speed (c_k) is [51, 54-56]

$$c_k = \frac{B}{\sqrt{\mu_0 \langle \rho \rangle}} \tag{1}$$

where B , μ_0 and $\langle \rho \rangle$ are the magnetic field strength, magnetic permeability of a vacuum and plasma density averaged within a spatial pixel, respectively. This equation shows that the field strength can be directly calculated once the phase speed and density are known.

To calculate the phase speed and plasma density, we utilized the wave tracking procedure that was developed around 2007 and further improved in the past decade [48, 49, 51, 56, 59], and the same line ratio method for density diagnostic

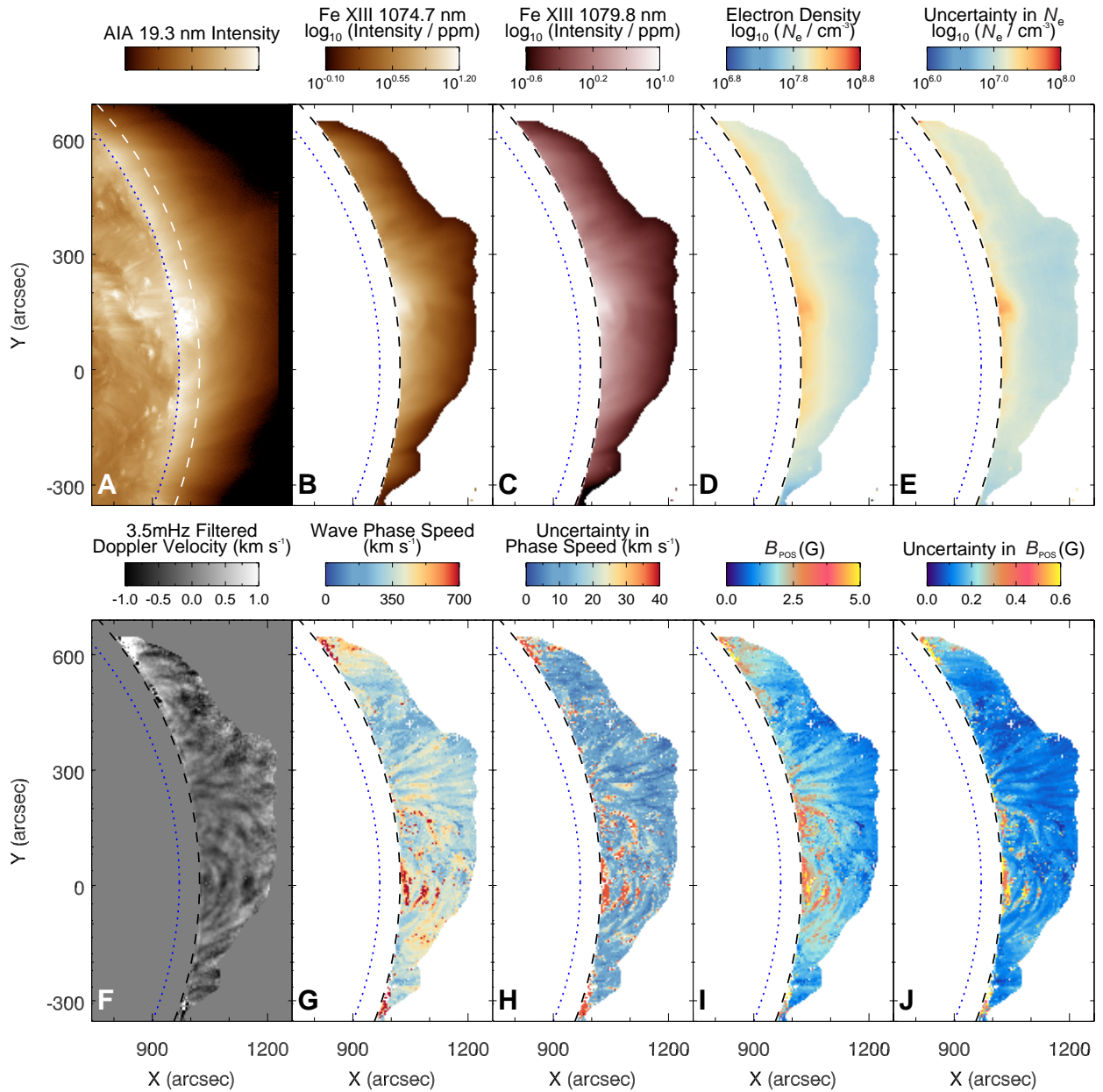


Figure 2 Analysis results for the observation on November 3, 2016 (dataset D2). The dotted and dashed curves mark the solar limb and the inner boundary of the CoMP FOV, respectively. (A) The AIA 19.3 nm image taken at 20:00:07 UT. (B)(C): The intensity maps of Fe XIII 1074.7 nm and 1079.8 nm. (D)-(E): The maps of electron number density and its uncertainty. (F): The filtered Doppler velocity map at 20:34:54 UT. (G)-(H): The maps of phase speed and its uncertainty. (I)-(J): The maps of derived B_{POS} and its associated uncertainty.

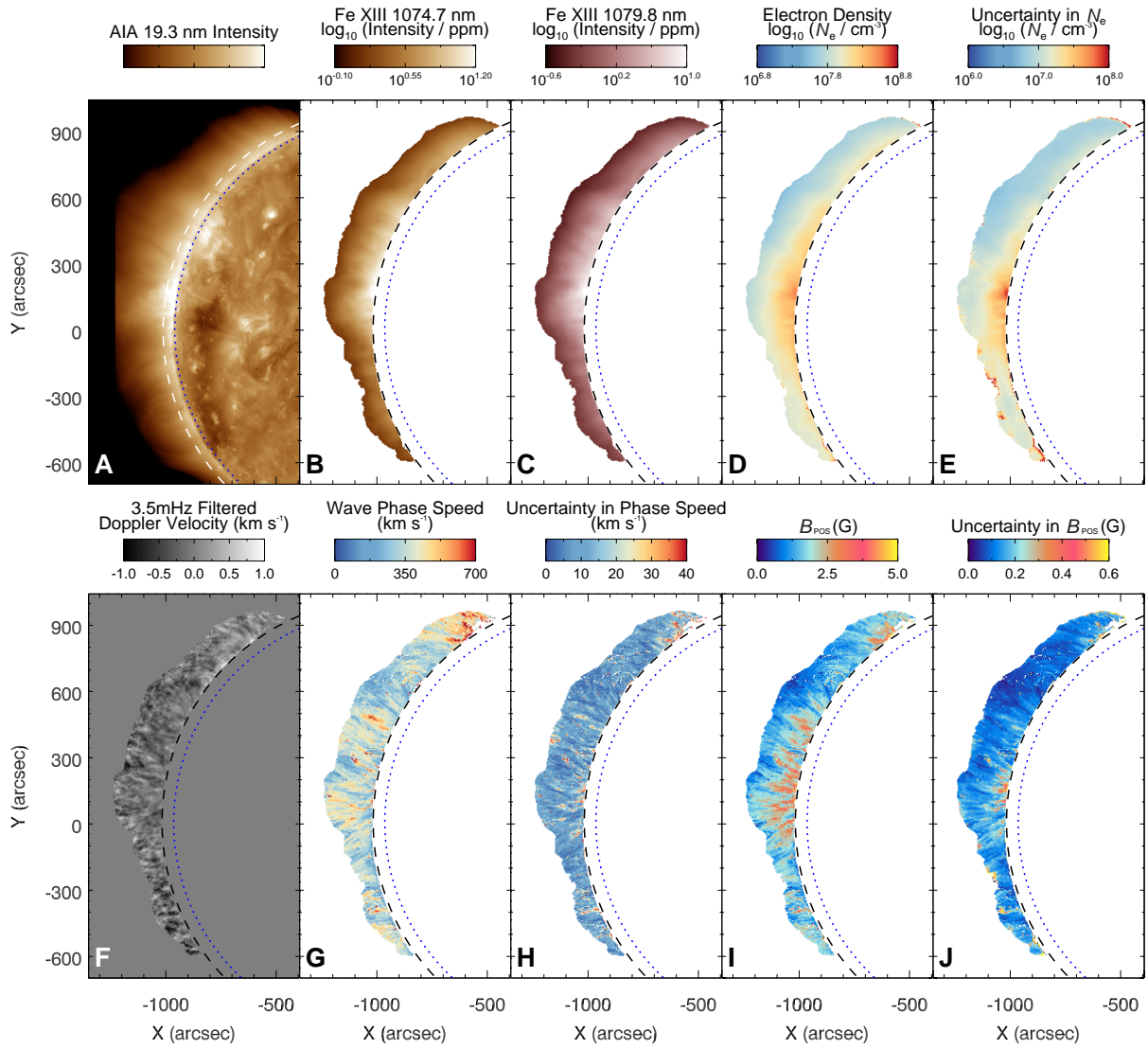


Figure 3 Same as Figure 2, but for the observation on March 20, 2017 (dataset D3).

in our previous work [56]. Detailed descriptions of these methods and estimations of the associated uncertainties can be found in the publications mentioned above. Here we just briefly describe the diagnostic procedures and present the results.

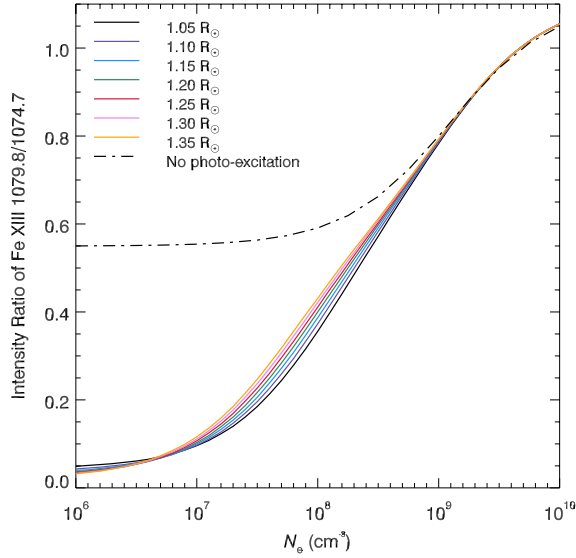


Figure 4 The theoretical relationship between line ratio and electron density. The dot-dashed curve is the result without consideration of photo-excitation. The colored solid curves show results at different heights when taking into account both collisional excitation and photo-excitation.

The intensity ratio of the Fe XIII 1079.8 nm / 1074.7 nm line pair is known to be sensitive to electron density (N_e). We utilized the CHIANTI database version 9.0 [60, 61] to generate the theoretical relationship between the Fe XIII 1079.8/1074.7 line ratio and electron density in the range of $1.05 R_\odot$ to $1.35 R_\odot$, considering both collisional excitation and photo-excitation. To include photo-excitation, a uniform spherical blackbody radiation source with a typical solar surface temperature is assumed [62]. Figure 4 shows the theoretical curves at several heights. As a comparison, the theoretical curve without consideration of photo-excitation is also plotted. From these theoretical curves, we obtained maps of the electron number density and the associated uncertainty. The results are presented in our previous work [56] (dataset D1) and in Figure 2(D)-(E) (dataset D2) and Figure 3(D)-(E) (dataset D3). Results from all datasets show that the electron number density mostly falls in the range of $10^{7.5} - 10^{8.5} \text{ cm}^{-3}$. Considering the typical coronal composition, the average plasma mass density ($\langle \rho \rangle$) can be calculated as $1.2N_e m_p$, where m_p is the proton mass (e.g., [44]).

The phase speed is obtained through the wave tracking procedure. For each spatial pixel, we first interpolated the Doppler velocity time series to achieve a 30-s regular ca-

cence, then filtered the interpolated time series to extract the 3.5-mHz (1.5-mHz FWHM) component. After that, a 41×41 pixel box was assigned around each spatial pixel, and the coherence between the time series at this and surrounding pixels was calculated. The high coherence region is usually elongated, and the orientation of its elongation was defined as the wave propagation direction/angle. After performing this calculation for all pixels, we can obtain a map of wave propagation angle. For the purpose of comparison, we also calculated the magnetic azimuth from linear polarization observations using the following equation

$$\phi = \frac{1}{2} \tan^{-1}\left(\frac{U}{Q}\right) \quad (2)$$

The linear polarization measurements have an intrinsic 180° ambiguity. Figure 5 shows the maps of wave propagation angle and magnetic azimuth for dataset D1. Similar maps for datasets D2 and D3 are depicted in Figure 6. Both the wave propagation direction and magnetic azimuth were measured relative to the east-west direction and are restricted within the range of -90° and 90° due to the 180° ambiguity. In the maps of magnetic azimuth, we only show pixels with a linear polarization degree greater than 0.06, because a lower linear polarization degree is subject to a greater uncertainty in the calculated azimuth [63]. The patterns of wave propagation angle and magnetic azimuth are generally similar for all the three datasets, suggesting that both parameters could provide information on the POS direction of the magnetic field. However, distinct differences are seen at several locations, especially locations where apparent loop structures are present, e.g., y positions of $-100''$ to $200''$ in Figure 6(A). In these regions, the wave propagation directions are generally consistent with the loop structures visible in the corresponding AIA intensity images. Note that the abrupt changes of wave propagation angles at some pixels in these regions are actually caused by the 180° ambiguity of wave angle, e.g., wave angles with values close to -90° and 90° actually represent similar wave propagation directions. In some parts of these regions, the angle between the local magnetic field and the solar radial direction could exceed the Van Vleck angle (54.74° , [64]), and thus the measured azimuth is subject to the 90° Van Vleck ambiguity. This effect appears to be responsible for some differences between the calculated wave angle and magnetic azimuth.

Based on the derived wave angles, a wave propagation path with a 31-pixel length can be traced for each pixel. The white curve in Figure 6(A) is an example of the traced wave path. A space-time diagram along each wave path was then constructed. A k - ω diagram was obtained by a fast Fourier transform (FFT) to the space-time diagram. Two branches of the

k - ω diagram correspond to waves that propagate outward and inward. Previous works have shown that the power of the outward propagating wave often dominates over the inward wave, resulting in a less accurate determination of the phase speed of inward wave (e.g., [49, 65]). Therefore, we applied an inverse FFT only to the negative-frequency part of the k - ω diagram, and obtained a space-time diagram for the outward wave (e.g., Figure 7(A)). A cross correlation of the time series at the center of the path with those at other locations on the path was calculated, resulting in a scatter plot showing the time lag at different locations (e.g., Figure 7(B)). Finally, a linear fitting was applied to the scatter plot to estimate the phase speed and its associated uncertainty. Snapshots of the Doppler velocity image sequences and the wave tracking results for datasets D2 and D3 are presented in Figure 2(F)-(H) and Figure 3(F)-(H), respectively. The phase speeds are mostly in the range of 300 to 700 km s⁻¹, similar to those in dataset D1 [56].

By substituting the derived density and wave phase speed

into eq. (1), we obtained the magnetic field strength. Since the measured phase speed is the component of the phase speed in the POS, the derived field strength is also the POS component. Figure 2(I)-(J) and Figure 3(I)-(J) show the maps of derived field strengths and associated uncertainties for datasets D2 and D3. The field strengths are mostly 1-5 Gauss and the uncertainties are generally smaller than 15%, comparable to those in dataset D1 [56]. The obtained field strengths are consistent with some estimations of the coronal magnetic field at similar heights using other approaches (e.g., [19, 20, 66]). As mentioned in our previous work [56], due to the unknown distribution of electron density along the LOS, an additional uncertainty of ~12% might be present in our derived B_{POS} . It is also worth mentioning that the current wave tracking method only considers the fitting error when estimating the uncertainty in phase speed. This likely underestimates the uncertainties in phase speed and magnetic field strength at some locations.

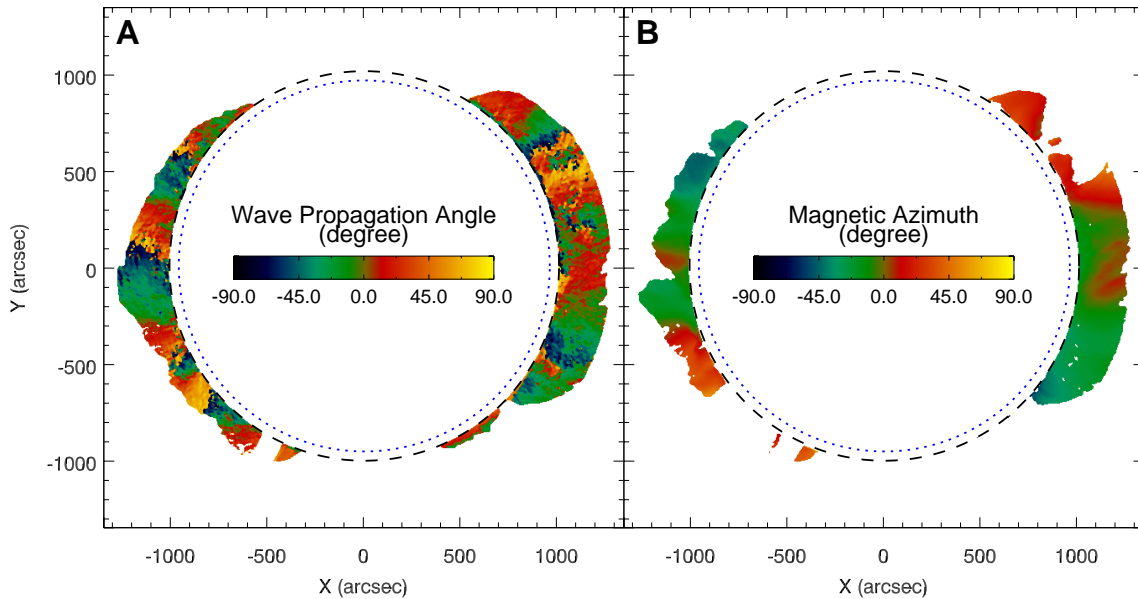


Figure 5 The maps of wave propagation angle (A) and magnetic azimuth (B) for the observation on October 14, 2016 (dataset D1). The dotted and dashed curves mark the solar limb and the inner boundary of the CoMP FOV, respectively. Pixels with a linear polarization degree lower than 0.06 have been removed from the azimuth map.

3.2 Distributions of coronal magnetic field strength and electron density

Histograms of the measured electron number density (N_e) and magnetic field strength (B_{POS}) in different height ranges for dataset D1 are presented in Figure 8. The red and blue histograms represent plasma parameters measured from two annulus sectors representing the quiet sun (QS) and another two annulus sectors enclosing active regions (ARs), respec-

tively. The two QS regions are located at the east limb. For the inner boundaries of these two annulus sectors, the ranges of y coordinates are from 394'' to 506'' and from -754'' to -428''. The two annulus sectors representing ARs are placed at the west limb. For their inner boundaries, the y positions are in the range of 54'' to 550'' and -598'' to -141''.

It is clear that both the electron density and magnetic field decrease with height, and that both are systematically lower

in the QS than in ARs. In addition, the difference between the QS and ARs becomes smaller as the height increases. We have also performed similar analyses for the other two datasets, and found a similar behavior.

To show the variations of N_e and B_{POS} with height, we chose the same annulus sectors mentioned above, and averaged the measured physical parameters within each $0.01 R_\odot$ height interval in the selected sectors. The height variations of the two parameters and associated standard errors on the mean values are shown in Figure 9. Several previous investigations (e.g., [66]) have shown that the variations of the coronal density and magnetic field with height follow a power-law function. Thus, we performed a simple power-law fitting to each measured curve in Figure 9. For both the electron density and magnetic field strength, a larger power-law index has been found in ARs than in the QS, indicating a stronger decrease in ARs. Analyses of the other two datasets have also yielded a similar result.

For comparison we also show results from two density

models [67, 68] in Figure 9(A) and (B). Our measured QS densities appear to be similar to the Leblanc model. The density values from the Newkirk model are several times larger than those in our measurements for both the QS and ARs. However, several recent off-limb observations of the inner corona have provided density values similar to our measurements [69-72]. Also, different active regions could have very different densities, which may partly explain the discrepancy between these measurements and the Newkirk density model.

The measured coronal magnetic field strengths are mostly 1-4 G in the height range of $1.05-1.35 R_\odot$. Our derived field strengths are consistent with results from some previous measurements using other techniques. For example, shock observations have revealed field strengths of 1.3-1.5 G in the height range of $1.3-1.5 R_\odot$ [20] and 1.7-2.1 G in the range of $1.1-1.2 R_\odot$ [66]. And a spectropolarimetric measurement has yielded a field strength of ~ 4 G above an active region at the height of $1.1 R_\odot$ [19].

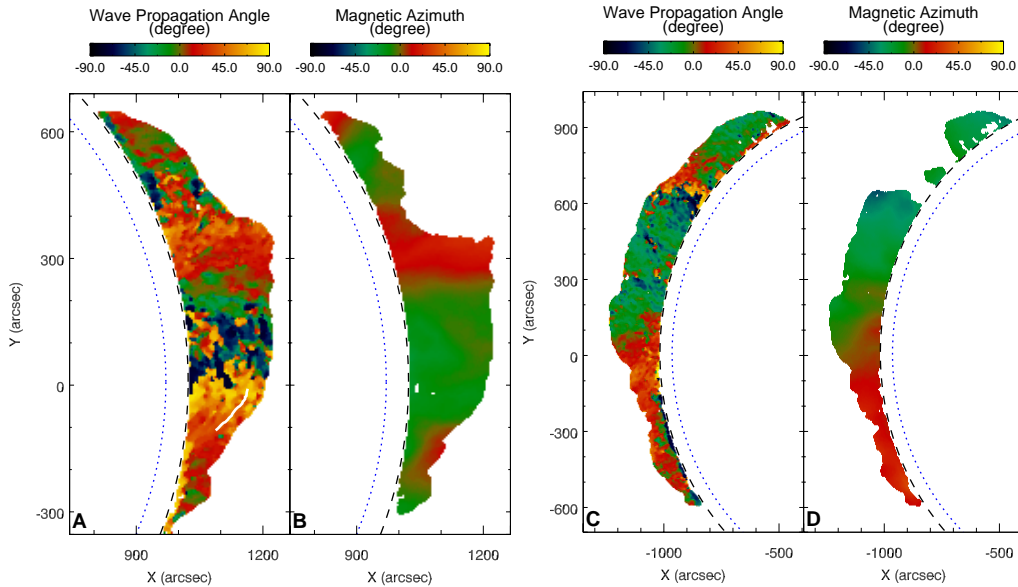


Figure 6 Same as Figure 5, but for datasets D2 (A-B) and D3 (C-D). The white curve in panel A shows a sample wave path used for the calculation of phase speed in Figure 7.

4 Discussion

Previous measurements of the coronal magnetic field through magnetoseismology normally provided an estimate of only the average field strength or 1D distribution of field strength along an oscillating structure. By applying the technique of magnetoseismology to the pervasive propagating transverse waves observed with CoMP, we now can obtain 2D distribu-

tions of the coronal magnetic field (coronal magnetograms), thus marking a leap forward in the application of magnetoseismology. Our analysis demonstrates that both the strength and direction of the coronal magnetic field in the POS can be obtained through actual coronal observations, filling the missing part of the measurements of the Sun’s magnetism.

Our technique relies on density diagnostics and wave tracking. For wave tracking, we need to perform a continuous

observation of the stronger Fe XIII 1074.7 nm line for ~1 hour or longer. During this period, normally the Fe XIII 1079.8 nm line could not be observed with CoMP. Thus, additional time is required to observe both Fe XIII lines for density diagnostics. In many CoMP observations the Fe XIII 1079.8 nm line was not used or had a S/N too low to allow a reliable density diagnostic. In such cases, it is still possible to obtain the density using simultaneous observations of the polarized brightness (e.g. [37]) with instruments such as K-Cor.

The ubiquitous propagating transverse waves observed with CoMP are identified as kink waves. It has been shown that when the length scale of the waveguide (i.e., radius of the flux tube) is much smaller than the wavelength, the kink wave is nearly incompressible and the restoring force is dominated by magnetic tension [51, 73, 74]. This indicates that the kink wave is of Alfvénic nature at the limit of long wavelength or thin flux tube, which should be the case in our observations. Therefore, these ubiquitous transverse MHD waves are sometimes also called Alfvénic waves (e.g., [44, 49, 51, 53, 54, 75]).

From maps of the wave propagation angle, we see abrupt changes of the angle at several locations. As mentioned in Section 3, some of these abrupt changes (e.g., around $y=100''$ in Figure 5(A), $y=0''$ in Figure 6(A), $y=600''$ in Figure 6(C)) are related to the 180° ambiguity, i.e., angles around $+90^\circ$ and -90° are actually similar angles, thus do not affect the determination of the wave propagation paths and the subsequent calculation of the phase speeds. Some other abrupt changes (e.g., around $y=350''$ in Figure 6(C)) are likely related to the complication by possible superimposition of different magnetic structures along the LOS or the low S/N. An anomalous angle may result in an obvious change in the direction of a constructed wave propagation path, meaning that different parts of the constructed path could trace adjacent magnetic field lines. However, from the Doppler velocity image sequence, we can see that the ubiquitous transverse waves often show coherent propagation across at least a few pixels, suggesting that adjacent field lines have similar directions and that waves propagate at similar speeds along adjacent field lines. Considering this, we expect that these anomalous angles may have a limited impact on the calculated phase speeds. We examined several locations of such abrupt changes in wave angles, and found that the extracted wave propagating paths are generally consistent with the loop structures visible from the intensity images, confirming the robustness of our results. A third group of abrupt changes in the maps of wave angle appear near the inner boundary of the FOV (e.g., around $y=450''$ in Figure 6(A)). Since there are not enough data points below a near-boundary pixel, the determination of the wave propagation angle at this pixel from the coherence calculation is likely subject to a large uncer-

tainty or even untrustworthy. In addition, there is increased uncertainty near the lower boundary due to guiding errors that cause increased noise just outside the occulting disk. These could result in an obvious deviation of part of the constructed wave path from the actual wave propagation direction. Thus, the calculated wave angles and phase speeds at some locations near the inner boundary should be treated with caution.

Due to some issues with both the wave propagation angle (abrupt changes of wave angle at some locations) and magnetic azimuth (Van Vleck ambiguity and large uncertainty in regions of weak linear polarization), we suggest to use both maps to accurately infer the POS direction of coronal magnetic field. A combination of the two maps allows us to correctly determine the magnetic field directions in regions with less accurate measurements of the wave propagation angle or magnetic azimuth.

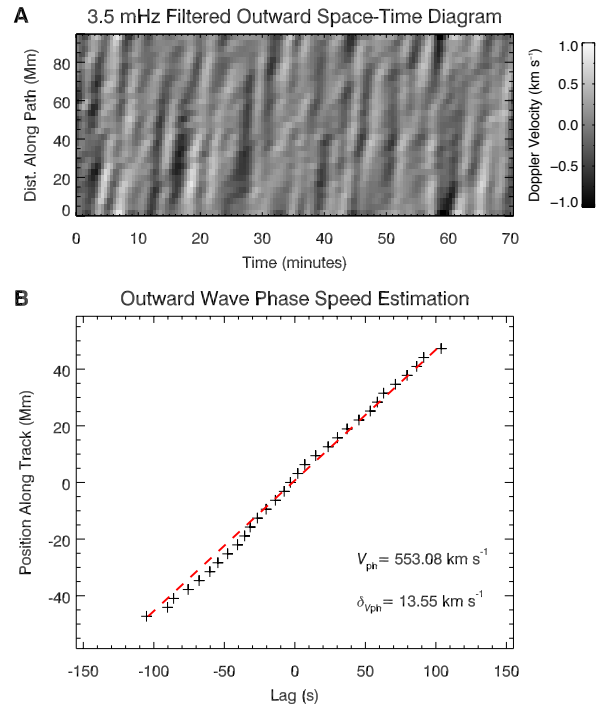


Figure 7 The calculation of phase speed. (A) Space-time diagram for the outward propagating wave along a sample path shown in Figure 6(A). (B) Estimation of the wave phase speed through a linear fitting to the scatter plot of position versus time lag.

We realize that the current method likely cannot provide magnetograms in coronal holes due to the very low S/N of the two Fe XIII lines. The Upgraded CoMP (UCoMP, [76]) instrument will observe emission from more spectral lines in a larger FOV. Some lines are expected to have emission in the lower-temperature coronal holes, and observations of them might allow us to map the coronal magnetic field in coronal

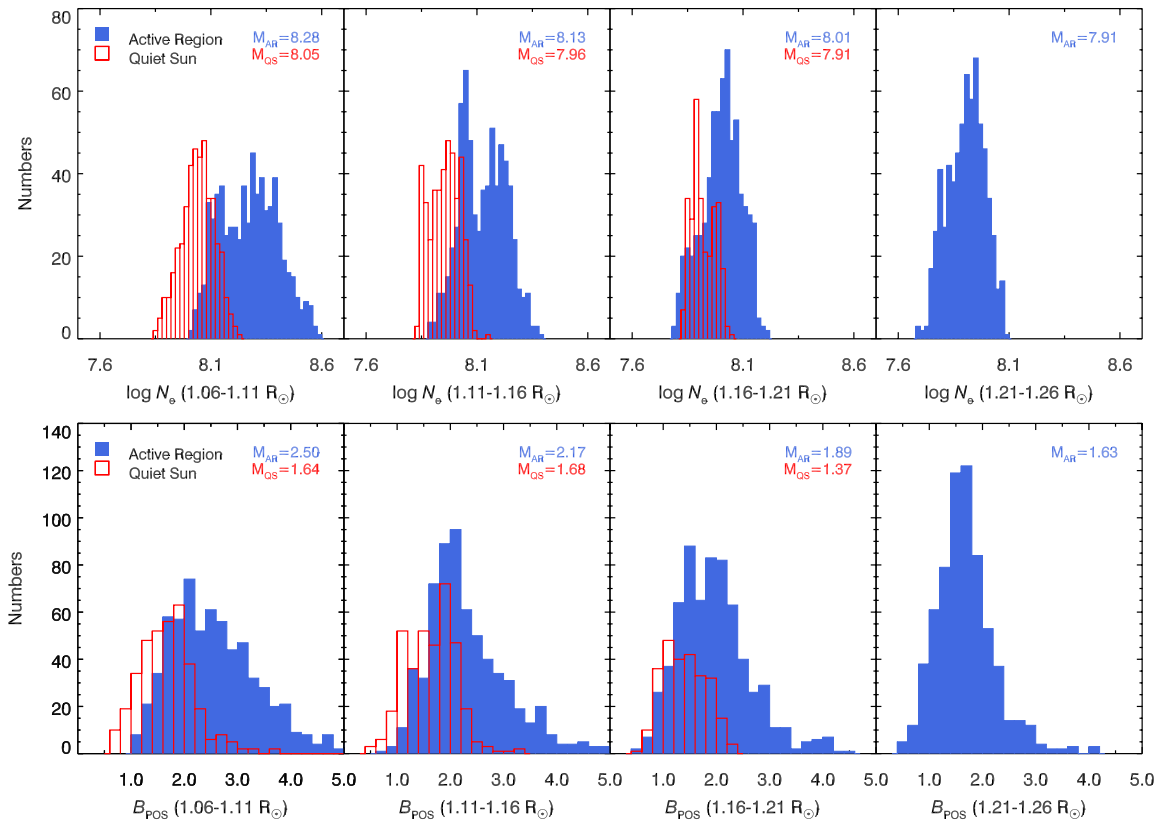


Figure 8 Distributions of the measured electron number density and POS magnetic field strength in different height ranges. The red and blue histograms are for the quiet Sun and active regions, respectively. Median values of parameters for the quiet Sun and active regions are represented by M_{QS} and M_{AR} , respectively.

holes. In addition, the higher spatial resolution of UCoMP observations will provide coronal magnetograms at a higher resolution.

With a much smaller FOV and higher spatial resolution, upcoming observations of the local coronal magnetic field from the Daniel K. Inouye Solar Telescope (DKIST, [77])

5 Summary

As a follow-up of our recent application of magnetoseismology in the measurements of the global coronal magnetic field [56], here we have obtained coronal magnetograms from more CoMP observations. Similar to our previous measurements, the electron number density and POS component of magnetic field in the height range of $1.05 R_{\odot}$ - $1.35 R_{\odot}$ have been found to be mostly $10^{7.5}$ - $10^{8.5} \text{ cm}^{-3}$ and 1-5 Gauss, respectively.

In addition, we have presented maps of the wave propagation direction derived through Stokes-I measurements and the magnetic azimuth derived from linear polarization observations. In general, each of these two maps can reliably reveal the POS distribution of the magnetic field orientation. A

will be complemented by CoMP-like observations of the global or large-scale coronal magnetic field. Moreover, by combining our measurements of the POS field and DKIST measurements of the LOS field through Zeeman effect, information on the coronal vector magnetic field could be obtained.

combination of these two independent measurements could resolve different uncertainties in the determination of the field direction at some locations.

We have also plotted distributions of the measured electron density and magnetic field strength, and compared their variations with height in the quiet Sun and active regions. A stronger decrease has been found in active regions than in the quiet Sun.

These results demonstrate the great potential of spectroscopic observations with CoMP-like instruments in routine measurements of the coronal magnetic field. Together with simultaneously measured photospheric magnetograms, such coronal magnetograms could provide critical information to advance our understanding of the magnetic coupling between different atmospheric layers as well as the physical mecha-

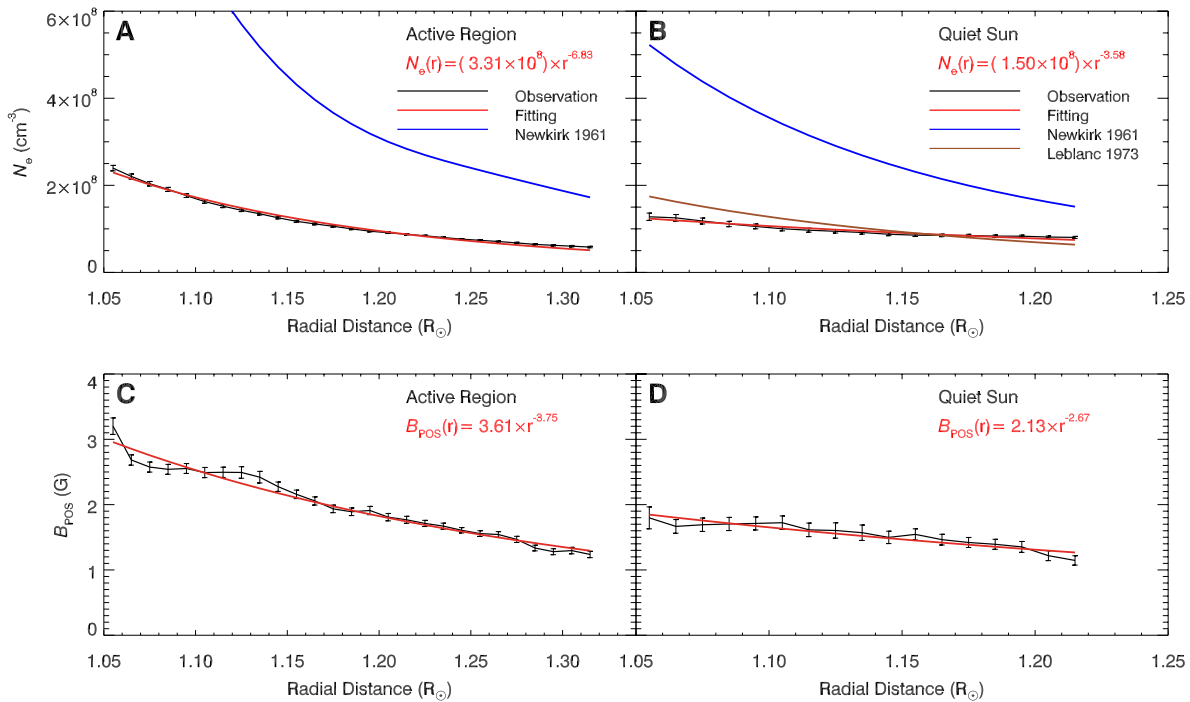


Figure 9 Variations of the measured electron number density (A-B) and POS magnetic field strength (C-D) with height. The black curves and error bars represent measurement results. The red curves show power-law fitting results. The fitting function is also shown in each panel. Results from two density models [67,68] are also presented for comparison.

nisms responsible for many types of dynamics in the solar atmosphere.

This work is supported by NSFC grants 11825301, 11790304(11790300), Strategic Priority Research Program of CAS (grant XDA17040507), and grant 1916321TS00103201. This material is based upon work supported by the National Center for Atmospheric Research, which is a major facility sponsored by the National Science Foundation under Cooperative Agreement No. 1852977. CoMP is an instrument operated by the National Center for Atmospheric Research. AIA is an instrument on SDO, a mission of NASAs Living With a Star Program.

- 1 Scherrer P H, Schou J, Bush R I, et al. The helioseismic and magnetic imager (HMI) investigation for the solar dynamics observatory(SDO). *Sol Phys*, 2012, 275: 207–227
- 2 Samanta T, Tian H, Yurchyshyn V, et al. Generation of solar spicules and subsequent atmospheric heating. *Science*, 2019, 366: 890–894
- 3 Yan Y, Sakurai T. New boundary integral equation representation for finite energy force-free magnetic fields in open space above the Sun. *Sol Phys*, 2000, 195: 89–109
- 4 Su Y, van Ballegoijen A, Lites B W, et al. Observations and nonlinear force-free field modeling of active region 10953. *Astrophys J*, 2009, 691: 105
- 5 Wiegelmann T, Sakurai T. Solar force-free magnetic fields. *Living Rev Sol Phys*, 2012, 9: 5
- 6 Huang Z H, Xia L D, Nelson C J, et al. Magnetic Braids in Eruptions of a Spiral Structure in the Solar Atmosphere. *Astrophys J*, 2018, 854: 80
- 7 Xue Z, Yan X, Cheng X, et al. Observing the release of twist by magnetic reconnection in a solar filament eruption. *Nat Commun*, 2016, 7: 1–11
- 8 Zhu X, Wiegelmann T, Solanki S. Magnetohydrostatic modeling of AR11768 based on a SUNRISE/IMaX vector magnetogram. *Astron*

Astrophys, in press

- 9 Chen Y J, Tian H, Zhu X S, et al. Solar ultraviolet bursts in a coordinated observation of IRIS, Hinode and SDO. *Sci China Tech Sci*, 2019, 62: 1555–1564
- 10 Riley P, Linker J A, Lionello R. A comparison between global solar magnetohydrodynamic and potential field source surface model results. *Astrophys J*, 2006, 653: 1510–1516
- 11 Jiang J, Wang J X, Zhang J H, et al. What drives the solar magnetic cycle? *Chin Sci Bull*, 2016, 61: 2973–2985
- 12 Liu Y, Lin H. Observational test of coronal magnetic field models. I: Comparison with potential field model. *Astrophys J*, 2008, 680: 2
- 13 Casini R, White S M, Judge P G. Magnetic diagnostics of the solar corona: synthesizing optical and radio techniques. *Space Sci Rev*, 2017, 210: 145–181
- 14 Li H, Degl’Innocenti E L, Qu Z Q. Polarization of coronal forbidden lines. *Astrophys J*, 2017, 838: 69
- 15 Bak-Stešlicka U, Gibson S E, Fan Y H, et al. The magnetic structure of solar prominence cavities: new observational signature revealed by coronal magnetometry. *Astrophys J Lett*, 2013, 770: L28
- 16 Rachmeler, L A, Gibson, S E, Dove, J B et al. Polarimetric Properties of Flux Ropes and Sheared Arcades in Coronal Prominence Cavities. *Sol Phys*, 2013, 288: 617–636
- 17 Chen Y J, Tian H, Su Y N, et al. Diagnosing the magnetic field structure of a coronal cavity observed during the 2017 total solar eclipse. *Astrophys J*, 2018, 856: 21
- 18 Lin H S, Penn M J, Tomczyk S. A new precise measurement of the coronal magnetic field strength. *Astrophys J Lett*, 2000, 541: L83–L86
- 19 Lin H S, Kuhn J R, Coulter R. Coronal magnetic field measurements. *Astrophys J Lett*, 2004, 613: L177–L180
- 20 Gopalswamy N, Nitta N, Akiyama S, et al. Coronal magnetic field measurement from EUV images made by the solar dynamics observatory. *Astrophys J*, 2012, 744: 72
- 21 Tan B L, Yan Y H, Tan C M, et al. Microwave zebra pattern structures

- in the X2.2 solar flare on 2011 February 15. *Astrophys J*, 2012, 744: 166
- 22 Tan B L, Karlicky M, Meszarosova H, et al. Diagnosing physical conditions near the flare energy-release sites from observations of solar microwave type III bursts. *Res Astron Astrophys*, 2016, 16: 013
- 23 Feng S W, Chen Y, Li C Y, et al. Harmonics of solar radio spikes at metric wavelengths. *Sol Phys*, 2018, 293: 39
- 24 Miyawaki S, Iwai K, Shibasaki K, et al. Coronal magnetic fields derived from simultaneous microwave and EUV observations and comparison with the potential field model. *Astrophys J*, 2016, 818: 8
- 25 Gary D E, Chen B, Dennis B R, et al. Microwave and hard X-ray observations of the 2017 September 10 solar limb flare. *Astrophys J*, 2018, 863: 83
- 26 Anfinogentov S A, Stupishin A G, Myshyakov I I, et al. Record-breaking coronal magnetic field in solar active region 12673. *Astrophys J Lett*, 2019, 880: L29
- 27 Fleishman G D, Gary D E, Chen B, et al. Decay of the coronal magnetic field can release sufficient energy to power a solar flare. *Science*, 2020, 367: 278–280
- 28 Zhu R, Tan B L, Su Y N, et al. Microwave diagnostics of magnetic field strengths in solar flaring loops. *Sci China Tech Sci*, 2020, 63, in press
- 29 Chen B, Shen C, Gary D E, et al. Measurement of magnetic field and relativistic electrons along a solar flare current sheet. *Nature Astronomy*, 2020
- 30 Grumer J, Brage T, Andersson M, et al. Unexpected transitions induced by spin-dependent, hyperfine and external magnetic-field interactions. *Phys Scr*, 2014, 89: 114002
- 31 Li W X, Grumer J, Yang Y, et al. A novel method to determine magnetic fields in low-density plasma facilitated through accidental degeneracy of quantum states in Fe^{9+} . *Astrophys J*, 2015, 807: 69
- 32 Li W X, Yang Y, Tu B S, et al. Atomic-level pseudo-degeneracy of atomic levels giving transitions induced by magnetic fields, of importance for determining the field strengths in the solar corona. *Astrophys J*, 2016, 826: 219
- 33 Si R, Brage T, Li W X, et al. A First Spectroscopic Measurement of the Magnetic-field Strength for an Active Region of the Solar Corona. *Astrophys J Lett*, 2020, 898: L34
- 34 Nakariakov V M, Ofman L, DeLuca E E, et al. TRACE observations of damped coronal loop oscillations: implications for coronal heating. *Science*, 1999, 285: 862
- 35 Ofman L, Wang T J. Hinode observations of transverse waves with flows in coronal loops. *Science*, 2008, 482: L9–L12
- 36 Chen Y, Song H Q, Li B, et al. Streamer waves driven by coronal mass ejections. *Astrophys J*, 2010, 714: 644–651
- 37 Chen Y, Feng S W, Li B, et al. A coronal seismological study with streamer waves. *Astrophys J*, 2011, 728: 147
- 38 Chen F, Peter H. Using coronal seismology to estimate the magnetic field strength in a realistic coronal model. *Astron Astrophys*, 2015, 581: A137
- 39 Guo Y, Erdélyi R, Srivastava A K, et al. Magnetohydrodynamic seismology of a coronal loop system by the first two modes of standing kink waves. *Astrophys J*, 2015, 799: 151
- 40 Li L P, Zhang J, Su J T, et al. Oscillation of current sheets in the wake of a flux rope eruption observed by the Solar Dynamics Observatory. *Astrophys J Lett*, 2016, 829: L33
- 41 Li D, Yuan D, Su Y N, et al. Non-damping oscillations at flaring loops. *Astron Astrophys*, 2018, 617: A86
- 42 Su W, Guo Y, Erdélyi R, et al. Period increase and amplitude distribution of kink oscillation of coronal loop. *Sci Rep*, 2018, 8: 4471
- 43 Wang T J, Ofman L, Davila J M, et al. Growing transverse oscillations of a multistranded loop observed by SDO/AIA. *Astrophys J Lett*, 2012, 751: L27
- 44 Tian H, McIntosh S W, Wang T J, et al. Persistent Doppler shift oscillations observed with Hinode/EIS in the solar corona: Spectroscopic signatures of Alfvénic waves and recurring upflows. *Astrophys J*, 2012, 759: 144
- 45 Anfinogentov S A, Nakariakov V M, Nisticò G. Decayless low-amplitude kink oscillations: a common phenomenon in the solar corona? *Astron Astrophys*, 2015, 583, A136
- 46 Zhang Q M, Dai J, Xu Z, et al. Transverse coronal loop oscillations excited by homologous circular-ribbon flare. *Astron Astrophys*, 2020, 638, A32
- 47 Tomczyk S, Card G L, Darnell T, et al. An instrument to measure coronal emission line polarization. *Sol Phys*, 2008, 247: 411–428
- 48 Tomczyk S, McIntosh S W, Keil S L, et al. Alfvén waves in the solar corona. *Science*, 2007, 317: 1192
- 49 Tomczyk S, McIntosh S W. Time-distance seismology of the solar corona with CoMP. *Astrophys J*, 2009, 697: 1384–1391
- 50 Liu J J, McIntosh S W, De Moortel I, et al. On the parallel and perpendicular propagating motions visible in polar plumes: an incubator for (fast) solar wind acceleration? *Astrophys J*, 2015, 806: 273
- 51 Morton R J, Tomczyk S, Pinto R. Investigating Alfvénic wave propagation in coronal open-field regions. *Nat Commun*, 2015, 6: 7813
- 52 Morton R J, Tomczyk S, Pinto R. A global view of velocity fluctuations in the corona below $1.3 R_{\odot}$ with CoMP. *Astrophys J*, 2016, 828: 89
- 53 Morton R J, Weberg M J, McLaughlin J A. A basal contribution from p-modes to the Alfvénic wave flux in the Sun’s corona. *Nat Astron*, 2019, 3: 223
- 54 Magyar N, Van Doorselaere T. Assessing the capabilities of dynamic coronal seismology of Alfvénic waves through forward modeling. *Astrophys J*, 2018, 856: 144
- 55 Long D M, Valori G, Pérez-Suárez D, et al. Measuring the magnetic field of a trans-equatorial loop system using coronal seismology. *Astron Astrophys*, 2017, 603: A101
- 56 Yang Z, Bethge C, Tian H, et al. Global maps of the magnetic field in the solar corona. *Science*, 2020, 369: 694–697
- 57 Tian H, Tomczyk S, McIntosh S W, et al. Observations of coronal mass ejections with the Coronal Multichannel Polarimeter. *Sol Phys*, 2013, 288: 637–650
- 58 Lemen J R, Title A M, Akin D J, et al. The atmospheric imaging assembly (AIA) on the solar dynamics observatory (SDO). *Sol Phys*, 2012, 275: 17–40
- 59 McIntosh S W, De Pontieu B, Tomczyk S. A coherence-based approach for tracking waves in the solar corona. *Sol Phys*, 2008, 252: 321–348
- 60 Dere K P, Landi E, Mason H E, et al. CHIANTI an atomic database for emission lines. I. Wavelengths greater than 50 Å. *Astron Astrophys Suppl Ser*, 1997, 125: 149–173
- 61 Dere K P, Del Zanna G, Young P R, et al. CHIANTI an atomic database for emission lines. XV. Version 9, improvements for the X-ray satellite lines. *Astrophys J Suppl Ser*, 2019, 241: 22
- 62 Young P R, Del Zanna G, Landi E, et al. CHIANTI - An atomic database for emission lines. VI. Proton rates and other improvements. *Astrophys J Suppl Ser*, 2003, 144: 135–152
- 63 Tomczyk S. Measurement Errors for Coronal Magnetic Field Parameters. Coronal Solar Magnetism Observatory Technical Note No. 1, 2015
- 64 Van Vleck J H. On the quantum theory of the polarization resonance radiation in magnetic fields. *Proc Nat Acad Sci*, 1925, 11: 612
- 65 Tiwari, A K, Morton R J, Regnier S, McLaughlin J A. Damping of Propagating Kink Waves in the Solar Corona. *Astrophys J*, 2019, 876: 106
- 66 Kumari A, Ramesh R, Kathiravan C, et al. Direct estimates of the solar coronal magnetic field using contemporaneous extreme-ultraviolet, radio, and white-light observations. *Astrophys J*, 2019, 881: 24
- 67 Newkirk G Jr. The solar corona in active regions and the thermal origin of the slowly varying component of solar radio radiation. *Astrophys J*, 1961, 133: 983
- 68 Leblanc Y, Leroy J L, Pecantet P. Quiet corona density model for the last maximum of solar activity. *Sol Phys*, 1973, 31: 343–350

- 69 Doschek G A, Warren H P, Laming J M, et al. Electron densities in the solar polar coronal holes from density-sensitive line ratios of Si vii and S x. *Astrophys J*, 1997, 482: L109–L112
- 70 Del Zanna G. Extreme ultraviolet spectroscopy of the solar corona. University of Central Lancashire, UK. *PhD thesis*, 1999
- 71 Tripathi D, Mason H E, Dwivedi B N, et al. Active region loops: Hinode/Extreme-ultraviolet Imaging Spectrometer observations. *Astrophys J*, 2009, 694: 1256–1265
- 72 O’Dwyer B, Del Zanna G, Mason H E, et al. Hinode extreme-ultraviolet imaging spectrometer observations of a limb active region *Astron Astrophys*, 2011, 525: A137
- 73 Goossens M, Terradas J, Andries J, et al. On the nature of kink MHD waves in magnetic flux tubes. *Astron Astrophys*, 2009, 503: 213–223
- 74 Goossens M, Andries J, Soler R, et al. Surface Alfvén waves in solar flux tubes. *Astrophys J*, 2012, 753: 111
- 75 McIntosh S W, De Pontieu B, Carlsson M, et al. Alfvénic waves with sufficient energy to power the quiet solar corona and fast solar wind. *Nature*, 2011, 475: 477
- 76 Landi E, Habbal S R, Tomczyk S. Coronal plasma diagnostics from ground-based observations. *J Geophys Res Space Phys*, 2016, 121: 8237–8249
- 77 Tritschler A, Rimmele T R, Berukoff S, et al. Daniel K. Inouye Solar Telescope: High-resolution observing of the dynamic Sun. *Astron Nachrichten*, 016, 337: 1064